remote sensing

MDPI

Article

Interpretable Deep Learning for Forecasting *Camellia oleifera* Yield in Complex Landscapes by Integrating Improved Spectral Bloom Index and Environmental Parameters

Tong Shi [1], Shi Cao [2,*], Xia Lu [2], Lina Ping [2], Xiang Fan [2], Meiling Liu [1] and Xiangnan Liu [1]

[1] School of Artificial Intelligence, China University of Geosciences (Beijing), Beijing 100083, China; 2004230020@email.cugb.edu.cn (T.S.); liuml@cugb.edu.cn (M.L.); liuxn@cugb.edu.cn (X.L.)
[2] The Second Surveying and Mapping Institute of Hunan Province, Changsha 410004, China; luxia43210231@126.com (X.L.); nana7smile@126.com (L.P.); 15674811345@163.com (X.F.)
* Correspondence: 3204250002@email.cugb.edu.cn

Highlights

What are the main findings?

- An improved Isogenetic Systemic Bloom Index (ISBI) has been developed to capture the flowering intensity of *Camellia oleifera*.
- A SHAP-based Attention LSTM (SALSTM) model has been developed to realise a latent yield-stress framework. This model integrates phenological flowering signals with environmental stress factors while enhancing transparency regarding the model's feature and temporal weighting patterns.

What are the implications of the main findings?

- Integrating ISBI-driven phenological signals with environmental regulatory mechanisms, and incorporating biological process understanding into empirical models, thereby enhancing the transparency of yield estimation models based on remote sensing technology.
- The proposed "potential–stress" framework improves the generalizability of deep learning models across complex landscapes, enabling more reliable large-scale forecasting of perennial crop productivity.

Abstract

Camellia oleifera, a woody oil crop unique to China, plays a crucial role in alleviating the global pressure of edible oil supply and maintaining ecological security. However, it remains challenging to accurately forecast *Camellia oleifera* yield in complex landscapes using only remote sensing data. The aim of this study is to develop an interpretable deep learning model, namely Shapley Additive Explanations–guided Attention–long short-term memory (SALSTM), for estimating *Camellia oleifera* yield by integrating an improved spectral bloom index and environmental parameters. The study area is located in Hengyang City in Hunan Province. Sentinel-2 imagery, meteorological observation from 2019 to 2023, and topographic data were collected. First, an improved spectral bloom index (ISBI) was constructed as a proxy for flowering density, while average temperature, precipitation, accumulated temperature, and wind speed were selected to represent environmental regulation variables. Second, a SALSTM model was designed to capture temporal dynamics from multi-source inputs, in which the LSTM module extracts time-dependent information and an attention mechanism assigns time-step-wise weights. Feature-level importance derived from SHAP analysis was incorporated as a guiding prior to inform attention distribution across variable dimensions, thereby enhancing model transparency. Third, model performance was

Check for updates

Academic Editor: Kun Jia

Received: 25 November 2025
Revised: 31 December 2025
Accepted: 12 January 2026
Published: 23 January 2026

Copyright: © 2026 by the authors. Licensee MDPI, Basel, Switzerland. This article is an open access article distributed under the terms and conditions of the Creative Commons Attribution (CC BY) license.

evaluated using root mean square error (RMSE) and coefficient of determination (R^2). The result show that the constructed SALSTM model achieved strong predictive performance in predicting *Camellia oleifera* yield in Hengyang City (RMSE = 0.5738 t/ha, R^2 = 0.7943). Feature importance analysis results reveal that ISBI weight > 0.26, followed by average temperature and precipitation from flowering to fruit stages, these features are closely associated with *C. oleifera* yield. Spatially, high-yield zones were mainly concentrated in the central–southern hilly regions throughout 2019–2023, In contrast, low-yield zones were predominantly distributed in the northern and western mountainous areas. Temporally, yield hotspots exhibited a gradual increasing while low-yield zones showed mild fluctuations. This framework provides an effective and transferable approach for remote sensing-based yield estimation of flowering and fruit-bearing crops in complex landscapes.

Keywords: *Camellia oleifera*; phenology-driven modeling; yield estimation; attention mechanism; SHapley Additive exPlanations; LSTM

1. Introduction

The global supply of edible oils is under increasing pressure [1]. As one of the world's four major woody oilseed tree species, *Camellia oleifera* provides a sustainable forestry-based solution for alleviating constraints on edible oil production [2–4]. Accurate and timely yield estimation is essential for improving oil production efficiency and supporting supply–demand regulation [5]. However, the growth and yield of *C. oleifera* are jointly influenced by intrinsic biological traits, climatic variability, and field management practices, which introduces substantial challenges and uncertainties in large-scale yield estimation [6–8]. Consequently, there is a critical need to develop scalable and accurate estimation frameworks capable of producing high-resolution, spatially explicit yield maps [5,9,10].

Since the 1970s, remote sensing technologies have been increasingly applied to large-scale crop yield estimation owing to their broad spatial coverage, long-term observation capability, and cost-effectiveness [9,11,12]. Satellite platforms such as Landsat [13,14], MODIS [15,16], Sentinel-2 [17], and Gaofen series [18] have been widely used for agricultural monitoring. By providing multi-temporal and multi-resolution imagery, these platforms enable phenological characterization and support crop yield assessment at regional to global scales. Existing remote sensing-based yield estimation approaches can be broadly classified into two categories: crop growth models and data-driven models [19–21].

Crop growth models simulate yield formation by integrating the combined effects of multiple factors, including crop traits, meteorological conditions, soil properties, and field management practices. These models quantitatively represent key physiological processes such as photosynthesis, transpiration, nutrient uptake, and biomass accumulation throughout the crop growth cycle. By explicitly characterizing crop–environment interactions at different growth stages, they enable dynamic prediction of yield formation [19]. Representative crop growth models include DSSAT [22], SWAP [23], APSIM [24], and WOFOST [25]. Despite their strong physical interpretability arising from explicit simulation of physiological processes, the practical application of crop growth models at regional or larger scales remains severely limited. These models rely heavily on extensive field observations and require numerous parameters that are difficult to obtain or calibrate across heterogeneous environments. Although data assimilation techniques have been introduced to incorporate remote sensing information into crop growth models, substantial parameter heterogeneity and scale mismatch persist, thereby constraining their robustness and transferability in large-scale yield estimation [26,27].

In contrast, data-driven models do not require prior knowledge of crop physiological processes. Instead, they infer complex nonlinear relationships between input features and yield from data samples, thereby establishing empirical linkages between remote sensing-derived indices and crop yield [5,28,29]. Commonly used indices include NDVI, EVI, GCVI, RVI, NPP, LAI, and SAVI [30–32]. A variety of machine learning algorithms, such as random forest (RF), support vector regression (SVR), and extreme gradient boosting (XGBoost), have been widely applied to yield prediction tasks [15,16,33]. Recurrent neural networks (RNNs) and long short-term memory (LSTM) networks further demonstrate strong capability in capturing temporal dependencies during crop growth [34,35]. In addition, numerous studies have shown that integrating multi-source data generally outperforms reliance on a single remote sensing input [9,36]. Despite their flexibility and strong predictive performance at regional scales, data-driven models typically suffer from limited structural interpretability. Model predictions are largely governed by statistical correlations rather than explicit representations of phenological or physiological mechanisms. Consequently, although satisfactory predictive accuracy can often be achieved, most data-driven approaches provide limited insight into how yield formation is regulated across different growth stages. This disconnect between predictive performance and biological interpretability has emerged as a fundamental bottleneck in remote sensing-based yield estimation and has stimulated growing interest in the development of interpretable modeling frameworks [37–39].

Despite the extensive application of RF, XGBoost, LSTM-based models, attention mechanisms, and post hoc explainability tools such as SHAP, several critical challenges remain unresolved in remote sensing-based yield estimation. Most existing approaches rely primarily on vegetation indices as indirect proxies for crop status, without explicitly modeling key phenological stages such as flowering that fundamentally determine yield formation potential. Although temporal deep learning models can improve predictive accuracy, they generally fail to disentangle phenology-driven yield potential from subsequent environmental stress regulation, resulting in limited physiological interpretability. Moreover, current interpretability strategies remain fragmented: attention mechanisms provide implicit feature weighting without explicit biological guarantees, whereas SHAP offers retrospective attribution that is decoupled from the model learning process, a limitation that is particularly pronounced under highly correlated multispectral inputs. Collectively, these unresolved issues underscore the need for yield estimation frameworks that explicitly integrate phenological signals with environmental regulation while embedding interpretability directly into the model structure.

Previous studies have demonstrated that flowering-related spectral information provides a direct and biologically meaningful link to yield formation. Flower abundance and flowering-stage spectral responses are strongly correlated with final yield, indicating that flowering characteristics are not merely supplementary indicators but key determinants of yield potential [40–42]. Advances in high-resolution satellite imagery and unmanned aerial vehicle (UAV) observations have enabled detailed monitoring of vegetation phenology [43], and a range of approaches has been proposed for extracting flowering characteristics, including classification-based spatial recognition methods and enhanced spectral index techniques [44–46]. For example, indices such as the Enhanced Bloom Index (EBI) have been successfully applied to detect flowering and estimate flower abundance in apricot orchards, providing critical inputs for subsequent yield modeling [47,48]. Dixon et al. combined PlanetScope and UAV imagery to predict forest flowering distributions using multispectral vegetation indices [49], while at larger spatial scales, Zang et al. developed a rapeseed flower recognition index based on MODIS data for regional flowering monitoring [50]. Fernando et al. developed the High-resolution Flowering Index (HrFI), enabling

highly accurate yield estimation for Brassica napus [51]. Despite these advances, robust detection and quantification of flowering signals remain challenging, particularly for crops characterized by sparse or light-colored flowers embedded within complex canopy backgrounds. Enhancing flower–leaf contrast while simultaneously suppressing background effects therefore remains a critical unresolved challenge.

Despite these advances, robust quantification of flowering signals from satellite imagery remains challenging, particularly under conditions of sparse flowering, light-colored petals, and complex canopy backgrounds. Conventional vegetation- or bloom-based indices often exhibit reduced sensitivity in the presence of strong background interference and demonstrate limited robustness when transferred across different sensors, canopy structures, or landscape contexts. These limitations are especially pronounced for perennial woody oil crops such as *Camellia oleifera*, whose white flowers are sparsely distributed within dense evergreen canopies. Consequently, there is a clear need for an improved spectral bloom index that enhances flower–leaf contrast while suppressing background vegetation effects, thereby enabling more reliable extraction of flowering intensity as a phenology-driven indicator of yield formation potential.

This study aims to embed a phenology-driven mechanism within an empirical modeling framework by using ISBI as a dominant variable and constructing a "potential–stress" yield estimation framework that integrates phenological signals with environmental regulation, thereby enhancing model interpretability and generalization. Specifically, the objectives of this study are to: (1) introduce an Improved Spectral Bloom Index (ISBI) to capture the flowering density of *Camellia oleifera*, serving as a key indicator of yield formation potential in the modeling process; (2) systematically incorporate critical meteorological factors between flowering and harvest, including precipitation, temperature, and wind speed, as regulatory variables to characterize the environmental response pathway of *C. oleifera* yield; and (3) develop a deep learning model, termed SALSTM, that integrates attention mechanisms with SHAP-based explanations to achieve dual interpretability across both variable and temporal dimensions.

2. Study Area and Data

2.1. Study Area

The study area is located in Hengyang City (110°32′16″–113°16′32″E, 26°07′05″–27°28′24″N), Hunan Province, China, which is one of the major production regions of *Camellia oleifera* (Figure 1a). In 2022, the total planting area reached 4.5447 million mu, with an annual camellia oil production of approximately 87,900 tons. The region is characterized by a subtropical humid monsoon climate, featuring distinct seasons, abundant thermal resources, and strong synchrony between rainfall and heat. The multi-year mean annual temperature ranges from 17.5 to 18.1 °C, with a frost-free period of approximately 298 days and more than 1500 h of annual sunshine. Mean annual precipitation is 1346.7 mm, distributed over an average of 161 rainy days.

Hengyang extends approximately 173 km from east to west and 150 km from north to south, covering a total area of 15,310 km^2. The terrain is dominated by hilly uplands (54.75%), followed by mountains and plains (approximately 21% each), while water bodies account for about 4% of the area (Figure 1b). Overall, the topography gradually declines from south to north, descending stepwise from the surrounding basins toward the central region. This complex spatial heterogeneity, together with pronounced phenological variability, provides a representative regional context for evaluating dynamic yield estimation of *C. oleifera* based on remote sensing.

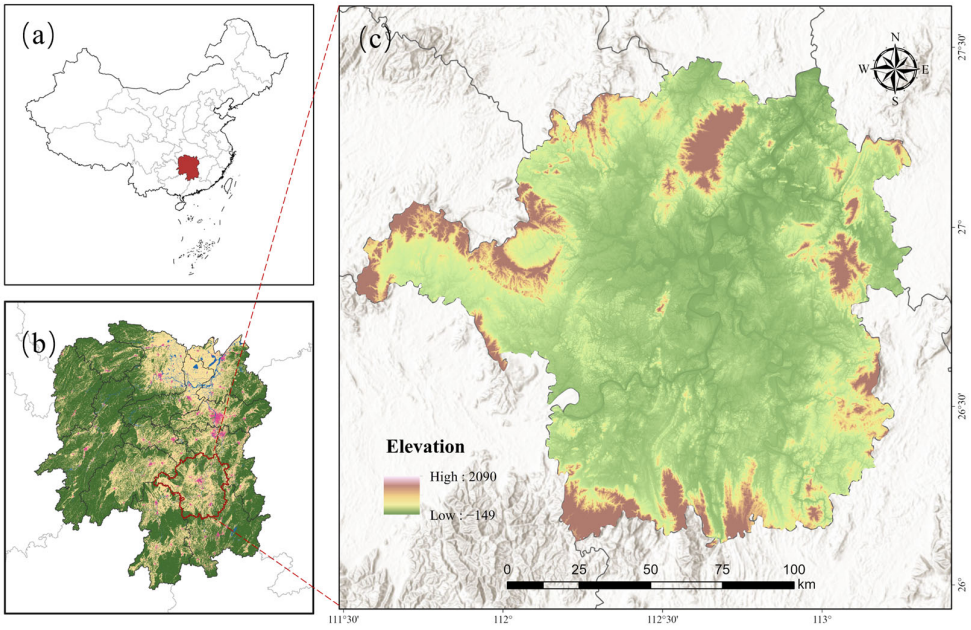


Figure 1. Geographic overview of the study area. (**a**) Location of Hunan Province within China. (**b**) Administrative boundaries and land-cover background of Hengyang City. (**c**) Topographic map of Hengyang City.

2.2. Data

We collected multi-source datasets covering *Camellia oleifera* production in Hengyang City from 2019 to 2023, resulting in a total of 800,225 plot-level samples. Yield observations for 2022 were obtained through field surveys conducted in representative plots across Changning District; these plot-level measurements (t/ha) served as high-resolution reference data for model calibration. For the remaining years, yield distributions were generated using a downscaling framework following Shirsath et al. [52], thereby enabling the construction of a consistent field-scale yield dataset spanning the period from 2019 to 2023.

Remote sensing inputs were derived from the Sentinel-2 Multispectral Instrument (MSI). Vegetation indices widely used in agricultural remote sensing, including the Normalized Difference Vegetation Index (NDVI), Enhanced Vegetation Index (EVI), and Soil-Adjusted Vegetation Index (SAVI), were computed to characterize canopy greenness, leaf area, and soil background conditions [53]. Monthly averages of each index were extracted to construct multi-temporal feature sequences. Given that *Camellia oleifera* flowers are light-colored and sparsely distributed, we further refined the Enhanced Bloom Index (EBI) to develop an Improved Spectral Bloom Index (ISBI), which serves as a phenology-sensitive indicator closely associated with flowering intensity and, consequently, with yield potential.

Meteorological variables were obtained from the National Centers for Environmental Information (NCEI) surface observation network. Daily observations of air temperature (TEMP), precipitation (PRCP), and maximum wind speed (MXSPD) from stations across Hunan Province and surrounding regions were spatially interpolated to generate continuous raster surfaces, clipped to the study area, and aggregated into monthly statistics covering the period from January 2019 to December 2023, temperature values were converted to Celsius (°C), precipitation to millimeters (mm), while wind speed retained its original unit of knots (kn). All variables were standardized using a consistent cross-year rescaling procedure to ensure unit comparability across the analysis. These variables were used as dynamic regulatory factors influencing the growth and yield formation of *Camellia oleifera*.

Topographic information was derived from the 30-m Shuttle Radar Topography Mission (SRTM) Digital Elevation Model. Terrain slope (SLOPE, degrees) was extracted as a

static geographic variable representing local topographic variability relevant to *Camellia oleifera* cultivation. To represent multi-source features across time, each variable was expanded into a feature_month index, in which a given feature is indexed across 12 monthly observations. We refer to this combined dimension as the temporal feature index. An overview of the distributional characteristics of all input variables, including minimum, maximum, mean, and standard deviation, is provided in Table 1.

Table 1. Characteristics of data sets used for the study.

Category	Variable	Min	Max	Mean	Std Dev	Source
Satellite	ISBI	0.0496	0.8251	0.2191	0.2026	Sentinel-2
	NDVI	0.1652	0.7237	0.4863	0.1639	Sentinel-2
	EVI	0.1130	0.5438	0.3297	0.1225	Sentinel-2
	SAVI	0.1024	0.4609	0.2908	0.1032	Sentinel-2
Hydrological	TEMP (°C)	−4.8	39.5	19.1249	7.0253	NOAA-NCEI
	SUMT (°C)	816.9479	2680.2199	1818.7654	147.3820	NOAA-NCEI
	PRCP (mm)	0.7620	302.0063	142.0918	96.9172	NOAA-NCEI
	MXSPD (kn)	7.4138	15.6563	11.2002	2.2549	NOAA-NCEI
Topographical	SLOPE	1.3137	17.8663	7.1116	4.6285	SRTM

3. Methods

To establish a yield estimation framework for *Camellia oleifera* guided by the spatiotemporal characteristics of flowering phenology (Figure 2), this study first derived the Improved Spectral Bloom Index (ISBI) from Sentinel-2 imagery to characterize flowering intensity, which served as the dominant variable (Figure 2a). In parallel, a set of regulatory variables was introduced to capture distinct modes and magnitudes of influence on yield formation. Canopy-related indices (NDVI, EVI, and SAVI) were used to represent canopy structure and biomass status of *C. oleifera* [54,55]; meteorological variables (TEMP, PRCP, SUMT, and MXSPD) were incorporated to describe external environmental stresses [56]; and the topographic factor (SLOPE) was included to represent long-term constraints on site suitability (Figure 2b).

Subsequently, both dominant and regulatory variables were jointly input into an XGBoost model for prior learning, and SHAP was employed to evaluate the global importance of each feature. The resulting feature-importance vectors were normalized to obtain w_{SHAP} values [57], which were then embedded as prior constraints within the attention mechanism (Figure 2c) [58]. Monthly sample sequences were reconstructed by integrating dominant variables, regulatory variables, and statistical yield observations (Figure 2d). These sequences were fed into a long short-term memory (LSTM) network to extract hidden representations, after which SHAP-guided attention was applied to weight the hidden states and generate context vectors. The resulting context vectors were subsequently passed to a regression layer for yield prediction (Figure 2e). Finally, prediction accuracy and model interpretability were evaluated through quantitative validation and explanatory analyses (Figure 2f). Overall, this framework enables dual attention across both variable and temporal dimensions while supporting structurally interpretable yield modeling [59,60].

Previous studies have demonstrated that temperature and precipitation play critical roles in regulating physiological processes such as photosynthesis, respiration, and oil accumulation during the growth of *Camellia oleifera*, while also influencing pollen viability and subsequent fruit development. Strong wind events during the flowering period can induce flower and young fruit abscission, thereby leading to yield reduction. In addition, variability in accumulated temperature exerts a significant influence on the growth rhythm

and nutrient allocation of fruit trees, and excessive heat accumulation may disrupt normal fruit development and ultimately impair yield formation.

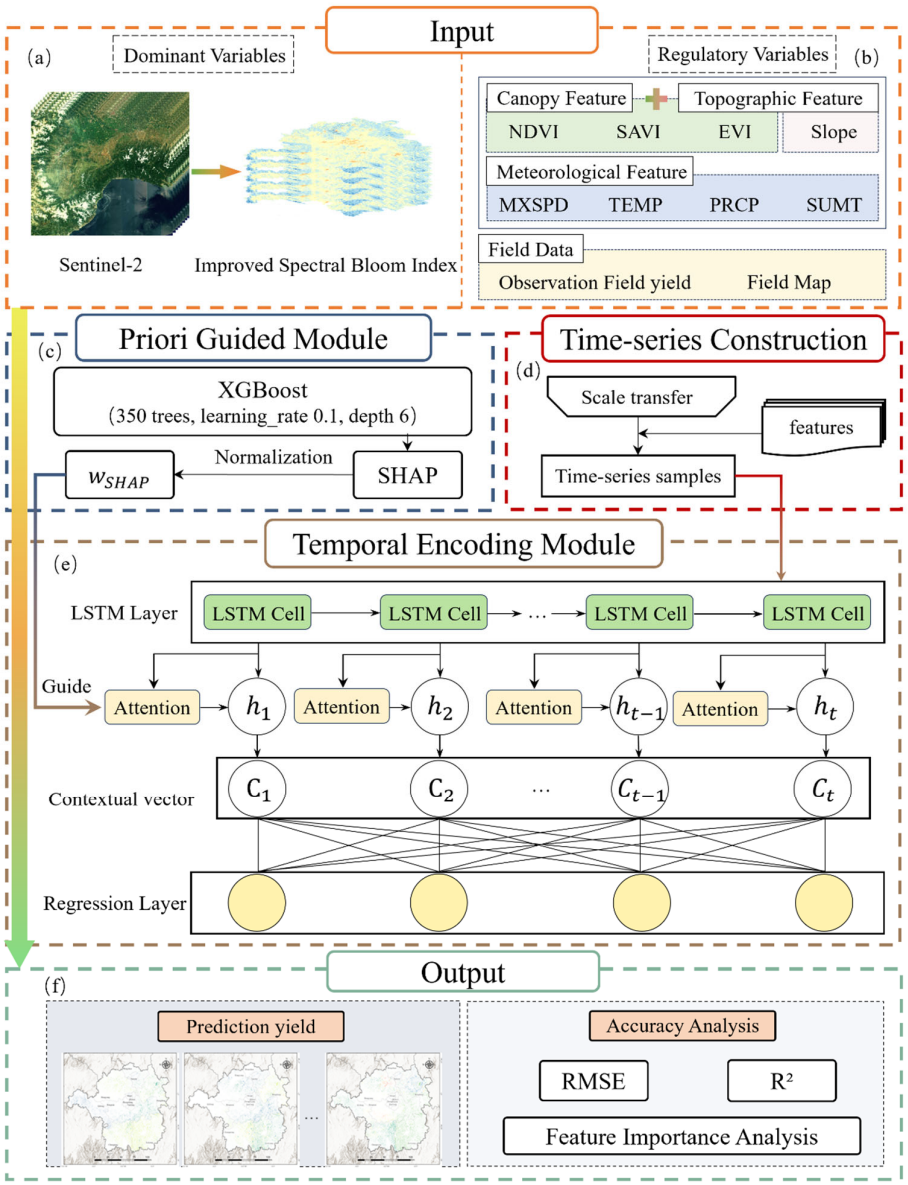


Figure 2. Schematic of the feature-importance-driven attention-enhanced LSTM prediction framework. (**a**) Extraction of ISBI from Sentinel-2 imagery. (**b**) Regulatory variables assembled from canopy, meteorological, and topographic features. (**c**) XGBoost–SHAP prior module generating normalized feature-importance vectors. (**d**) Construction of monthly time-series samples. (**e**) LSTM with SHAP-guided attention for temporal encoding and prediction. (**f**) Output results.

3.1. Construction of the Improved Spectral Bloom Index and Feature Time-Series

We assembled a plot-scale dataset of *Camellia oleifera* cultivation in Hengyang City for the period 2019–2023 to provide spatial constraints and parcel-level masks for deep learning-based modeling. Among these parcels, a subset from 2022 was associated with in situ yield measurements, which enabled regression modeling and accuracy assessment. To derive plot-level yield estimates for the remaining years, we adopted the crop-yield spatial downscaling approach proposed by Shirsath et al. [52], in which county-level statistical yields were fitted to high-resolution covariates including remote sensing, meteorological, and topographic factors, and subsequently disaggregated to parcel scales through

regression-based mapping. This procedure generated spatially explicit yield layers that served as supervisory variables for model training.

To characterize the environmental regulation of yield formation, both dynamic and static variables were extracted from three domains encompassing remote sensing, meteorology, and topography, and were standardized to harmonize modeling scales and spatial distributions.

To effectively capture canopy spectral dynamics at key stages of the *Camellia oleifera* growth cycle, Sentinel-2 multispectral imagery was employed. Image preprocessing included atmospheric correction and cloud masking, followed by monthly maximum-value compositing to generate a continuous remote-sensing time series. During feature construction, we extracted vegetation indices (such as NDVI, EVI and SAVI) that have been extensively validated for vegetation monitoring and yield estimation, and calculated their monthly averages to form multi-temporal feature vectors. However, because *C. oleifera* flowers are predominantly white and relatively sparse, their spectral signals are typically weak and easily confounded with the surrounding green canopy background, resulting in low sensitivity of the conventional Enhanced Bloom Index (EBI) during sparse flowering periods. To improve the detectability of white flower signals, this study proposes an Improved Spectral Bloom Index (ISBI), which enhances spectral contrast between visible and red-edge bands, thereby amplifying reflectance differences between flowers, characterized by high reflectance, and leaves, characterized by relatively low reflectance. Concurrently, a near-infrared normalization term is incorporated to suppress strong vegetation reflectance in the near-infrared band, reducing interference from both vegetation and soil backgrounds. As illustrated in Figure 3, the ISBI formulation strengthens the differentiation between floral and foliage spectra and refines the index structure relative to the original EBI. Calculated from Sentinel-2 multispectral imagery, the ISBI quantitatively characterizes the spatial distribution and density of flowers during the flowering period and serves as a phenology-driven variable for assessing yield formation potential in *Camellia oleifera*, reflecting the contribution of flowering intensity to subsequent yield formation processes. The formulation of ISBI is given as follows:

$$ISBI = \frac{R+G+B}{\left(\frac{G}{B}\right)\cdot(R-B+\theta)\cdot\left(\frac{NIR}{R+G+B}\right)} \quad (1)$$

where R, G, B and NIR denote the reflectance values for the red, green, blue and near-infrared bands, respectively, and θ is an adjustment constant to ensure the denominator remains non-negative.

To construct meteorological time-series features aligned with the spatial and temporal domains of the remote-sensing inputs, ground-based observations from meteorological stations across Hunan Province and surrounding regions were integrated to extract key variables, including air temperature (TEMP), precipitation (PRCP), and maximum wind speed (MXSPD). Daily station observations were spatially interpolated using inverse distance weighting (IDW) to generate continuous meteorological fields, which were subsequently rasterized at a spatial resolution of 1 km. These raster layers were clipped and masked to match the spatial extent of the remote-sensing data. Daily meteorological fields were then aggregated to the monthly scale to derive maximum, minimum, and mean values, as well as accumulated temperature (heat units), thereby forming monthly meteorological time-series features. This procedure produced a continuous dataset spanning January 2016 to December 2023, which served as dynamic climatic regulators for model training.

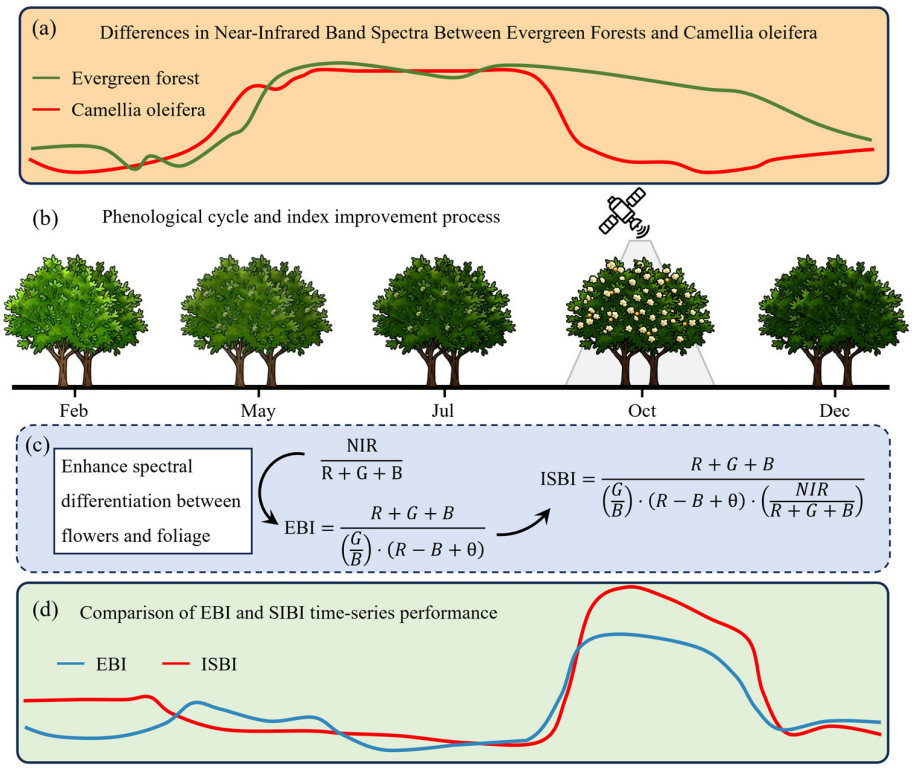


Figure 3. Conceptual framework for the enhancement of the Enhanced Bloom Index (EBI) into the improved spectral bloom index (ISBI). (**a**) Spectral contrast challenges between evergreen forests and *C. oleifera*. (**b**) Phenological stages and observable flowering window. (**c**) Conceptual derivation of ISBI from EBI through enhanced spectral separation. (**d**) Comparison of EBI and ISBI time-series responses during flowering.

To capture the regulatory effects of terrain on *Camellia oleifera* site suitability and yield variability, a digital elevation model (DEM) for Hengyang City and its derived slope were incorporated as static geographic features. The DEM has a spatial resolution of 30 m and was reprojected, resampled, and co-registered to align with the remote-sensing grids. Slope was computed using standard spatial analysis methods to represent local relief at the parcel scale. As a key topographic factor influencing plantation distribution and light conditions of *C. oleifera*, slope was included as a static input to enhance the model's capacity to capture yield variability under topographic heterogeneity.

3.2. Priori Guided Module

To mitigate overfitting in machine learning algorithms and reduce interference arising from multicollinearity among input variables [16], while simultaneously ensuring interpretability of feature importance, we selected the gradient boosting decision tree algorithm XGBoost (Extreme Gradient Boosting) as the regression model. XGBoost is trained using a greedy optimization strategy, in which regression trees are constructed sequentially, with each iteration aiming to minimize the residuals from the previous ensemble [61]. The model adopts an additive structure, whereby the final prediction is obtained through a weighted summation of the outputs from all individual trees, which can be expressed as follows:

$$\hat{y}_i = \sum_{k=1}^{K} f_k(x_i), f_k \in \mathcal{F} \quad (2)$$

where $\hat{y}_i$ denotes the predicted value of the i-th sample, f_k represents the k-th regression tree, $\mathcal{F}$ indicates the functional space of regression trees. Because each iteration incre-

mentally models the residuals from the preceding round, XGBoost effectively mitigates the destabilizing effects of collinear variables in high-dimensional feature spaces. This cumulative learning process not only enhances model robustness but also provides a solid basis for subsequent interpretability analysis using SHAP, allowing the extraction of both global and local feature importance.

XGBoost further constrains model complexity and suppresses overfitting by incorporating both L1 and L2 regularization penalties on the number of leaf nodes and their corresponding weights. Accordingly, the overall objective function of the model is defined as follows:

$$\mathcal{L} = \sum_{i=1}^{n} l(y_i, \hat{y}_i) + \sum_{k=1}^{K} \Omega(f_k), \Omega(f) = \gamma T + \frac{1}{2}\lambda \sum_{j=1}^{T} w_j^2 \quad (3)$$

where $l(\cdot)$ denotes the prediction error term, while $\Omega(f_k)$ represents the complexity penalty of the k-th regression tree. Specifically, T is the number of leaf nodes, w_j denotes the weight, γ and λ are the regularization coefficients. In addition, XGBoost employs parallelization techniques in critical processes such as feature splitting and node pruning, while enhancing training efficiency through block-structured feature storage and sparse-aware algorithms, making it highly suitable for complex remote sensing yield estimation scenarios.

SHAP (SHapley Additive exPlanations) is a game-theoretic framework for interpreting machine learning predictions by quantifying the marginal contribution of each input feature to the model output based on Shapley values [57]. In regression tasks, the SHAP value for a given feature is defined as the difference between the expected model output with and without that feature, thereby representing its contribution to the final prediction. Formally, the SHAP value can be expressed as follows:

$$\phi_j^{(i)} = f(x_i) - E[f(x)] \quad (4)$$

where $\phi_j^{(i)}$ denotes the SHAP value of feature j for sample i, $f(x_i)$ represents the model's prediction for that sample, and $E[f(x)]$ indicates the average prediction across all samples.

In this study, the TreeSHAP explainer was applied to the trained XGBoost model to compute SHAP values for all input variables across samples. The global importance of each feature was then quantified as the mean absolute SHAP value over all samples. Let ϕ_i denote the SHAP value of feature i; its global importance score is calculated as follows:

$$I_i = \frac{1}{N} \sum_{j=1}^{N} \left| \phi_i^{(j)} \right| \quad (5)$$

We normalize the feature importance vector $I = [I_1, I_2, \ldots, I_d]$ obtained from SHAP values to derive the guidance vector w_{SHAP}. This serves as the prior for initializing feature attention weights, thereby enhancing the model's ability to focus on key predictive factors.

In this section, yield-driving processes were modeled using the XGBoost algorithm, and feature importance was quantified through the SHAP method to provide prior knowledge for guiding and interpreting the subsequent attention mechanism. As illustrated in Figure 4, the XGBoost model iteratively constructs decision trees based on gradient optimization, after which SHAP is applied to evaluate the marginal contribution of each feature. This strategy not only improved the effectiveness of feature representation but also enhanced the interpretability and robustness of the overall yield estimation framework.

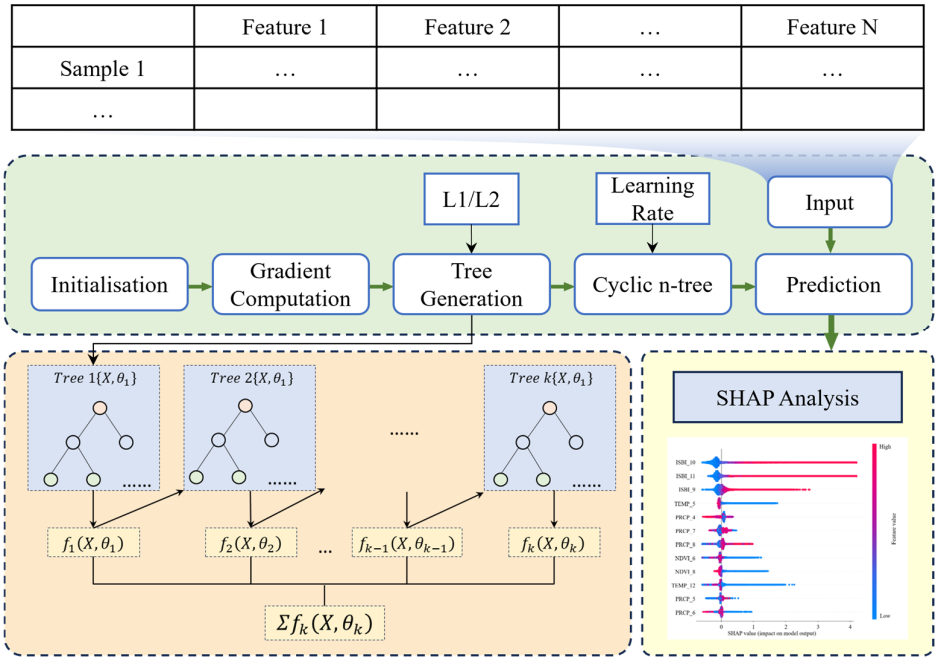


Figure 4. Schematic Diagram of XGBoost Model and SHAP Analysis.

3.3. Temporal Encoding Module

Long short-term memory (LSTM) is a specialized form of recurrent neural network (RNN) [62]. RNNs model sequential dependencies across time steps through hidden states, enabling the processing and retention of temporally evolving information; however, standard RNNs rely heavily on gradient propagation during backpropagation through time and are therefore susceptible to vanishing or exploding gradient problems. To address these limitations, Hochreiter and Schmidhuber proposed the LSTM architecture, which extends conventional RNNs by introducing gating mechanisms that dynamically regulate information flow, thereby improving the modeling of long-range temporal dependencies. Gers et al. subsequently incorporated a forget gate into the original design, further enhancing the flexibility and stability of the network [63]. The core of the LSTM architecture lies in the linear transmission path of the cell state, which serves as the primary conduit for information flow across time steps. At each time step, the cell state C*t* is regulated by three gates, each determining which information should be retained, updated, or discarded; each gate is implemented as a fully connected layer followed by a sigmoid activation function.

The forget gate determines which parts of the previous cell state (C_{t-1}) should be discarded. It processes the previous hidden output (h_{t-1}) together with the current input (x_t) through a fully connected layer with a sigmoid activation function σ, producing an output value (f_t) in [0,1]. When $f_t = 0$, all information in C_{t-1} is forgotten; when $f_t = 1$, all information in C_{t-1} is retained. where W_f is the weight matrix of the forget gate and b_f is its bias parameter:

$$f_t = \sigma\left(W_f \cdot [h_{t-1}, x_t] + b_f\right) \tag{6}$$

The input gate determines which information from the current input (x_t) is incorporated into the cell state for updating. This process involves two components. The first is the update ratio (i_t), obtained in a manner similar to the forget gate: h_{t-1} and (x_t) are passed through a fully connected layer with a sigmoid activation function σ. The second component is the candidate cell state ($\widetilde{C}_t$), produced by passing the same inputs through a fully connected layer with a *tanh* activation. The updated cell state (C_t) is then derived by combining the previous state (C_{t-1}), filtered through the forget gate, with the candidate

state ($\widetilde{C}_t$), weighted by the input gate. The operations are given as follows, where W_i and W_C are the weight matrices of the input gate and candidate state, and b_i and b_C are their respective bias terms:

$$i_t = \sigma(W_i \cdot [h_{t-1}, x_t] + b_i) \tag{7}$$

$$\widetilde{C}_t = \tanh(W_C \cdot [h_{t-1}, x_t] + b_C) \tag{8}$$

$$C_t = f_t \times C_{t-1} + i_t \times \widetilde{C}_t \tag{9}$$

The output gate determines the final output at the current time step. Specifically, (h_{t-1}) and (x_t) are passed through a fully connected layer with a sigmoid activation to produce an initial output gate value (o_t). This value is then multiplied elementwise with the *tanh*-transformed current cell state (C_t), yielding the hidden state (h_t) as the final output:

$$o_t = \sigma(W_o \cdot [h_{t-1}, x_t] + b_o) \tag{10}$$

$$h_t = o_t \cdot \tanh(C_t) \tag{11}$$

Although LSTM effectively captures internal dependencies within time series, it assumes equal weighting across input feature dimensions and thus cannot reflect differences in the relative contributions of variables to yield prediction. To address this limitation, a feature level attention mechanism is introduced on top of the LSTM encoder outputs (as illustrated in Figure 5) to adaptively reweight feature representations, enabling the model to allocate greater emphasis to relatively informative inputs during prediction.

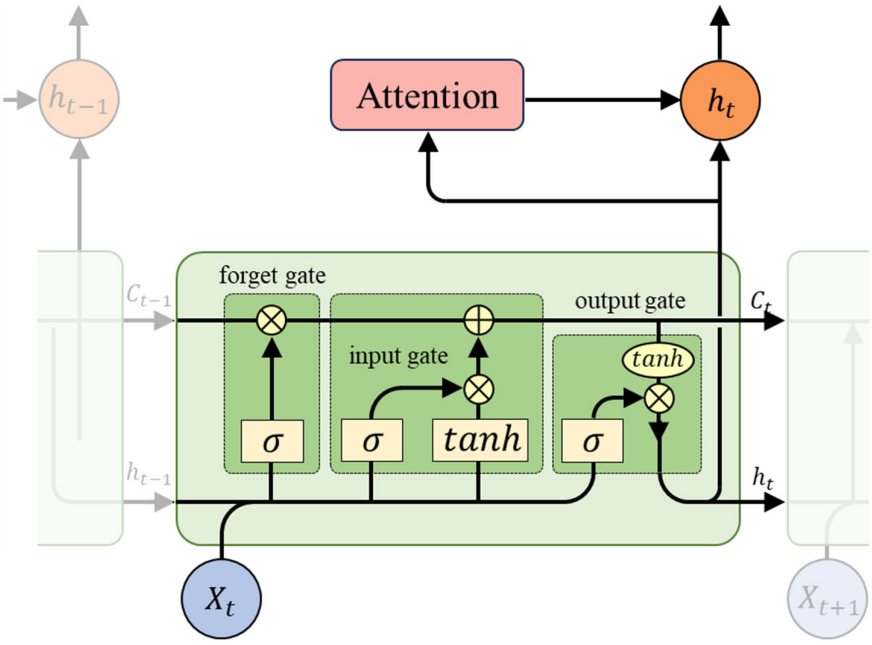


Figure 5. Schematic Diagram of an Attention Mechanism-Enhanced LSTM Architecture.

The attention mechanism enables a neural network to adaptively reweight input representations, allowing the model to focus on relatively informative of the input sequence. In this study, the mechanism follows the Transformer-style scoring and weighting based on queries (Query), keys (Key), and values (Value). For the hidden state vector output by the LSTM encoder at time step t, three learnable linear transformation matrices are applied, and the representations are obtained as follows:

$$Q_t = W_Q h_t \in R^d \tag{12}$$

$$K_t = W_K h_t \in R^d \tag{13}$$

$$V_t = W_V h_t \in R^d \tag{14}$$

where W_Q, W_K and W_V are learnable linear projection matrices, and d denotes the attention dimension. The attention score vector α_t is then computed to quantify the relative contribution of each feature dimension to the model's prediction at a given time step. The scaled dot-product scoring function is defined as follows:

$$\alpha_t = \text{Softmax}\left(\frac{Q_t \circ K_t}{\sqrt{d}}\right) \tag{15}$$

where the Softmax operation ensures that all attention scores are normalized within the [0, 1] interval, and $\odot$ denotes elementwise multiplication. Finally, the attention weights are applied to the value vector V_t to obtain the feature weighted context representation c_t:

$$c_t = \alpha_t \odot V_t \tag{16}$$

After aggregating the context vectors from all time steps $(C_1, \ldots, C_t)$, a global representation is formed and subsequently fed into the regression prediction layer.

To enhance the stability and consistency of the attention mechanism, the feature importance prior vector w_{SHAP}, derived from the preceding XGBoost–SHAP analysis, is introduced as a guiding inductive prior. During training, an auxiliary regularization loss is defined to constrain the discrepancy between the learned attention distribution α_t and the prior distribution w_{SHAP}, thereby encouraging the model to focus more closely on high-contribution features. The regularization are designed as follows:

KL-divergence-based regularization term:

$$\mathcal{L}_{\text{reg}}^{KL} = \sum_{t=1}^{T} D_{\text{KL}}\left(w^{\text{SHAP}} \parallel \alpha_t\right) \tag{17}$$

Finally, the total loss function of the model is composed of the regression prediction error term and the attention-guided regularization term:

$$\mathcal{L}_{total} = \mathcal{L}_{mse} + \lambda \cdot \mathcal{L}_{reg} \tag{18}$$

Here, λ is a hyperparameter that controls the strength of the regularization term. By incorporating the SHAP-based prior-guided attention mechanism, the model achieves dynamic focusing capability at the feature dimension while balancing predictive accuracy and structural interpretability.

In this study, all variables were organized at a monthly temporal resolution to construct continuous 12-month time-series data, forming a three-dimensional tensor $X \in \mathbb{R}^{N \times T \times F}$, where N denotes the number of samples, $T = 12$ represents the sequence length in months, and $d = 19$ corresponds to the number of features extracted per month.

3.4. Model Training

To achieve high-precision yield estimation, we developed a SALSTM model while systematically evaluating its performance by comparing multiple benchmark models, including linear regression (LR), support vector regression [64], artificial neural networks [65], random forests [66], gradient-boosted trees [61], long short-term memory networks and Attention-LSTM model without SHAP priors (ATLSTM). The multi-source sample set was partitioned into training, validation, and test subsets at a 70%/20%/10% ratio. To mitigate the impact of scale differences on training stability, all input features were standardized using Z-score normalization, with parameters fitted on the training set and consistently ap-

plied to the validation and test data. To assess the proposed SALSTM framework's stability across annual divisions, we additionally conducted year-by-year validation (LOYO). The model was trained using data from the preceding four years and tested against 2023 data.

The primary model adopts a dual-channel Attention-LSTM architecture incorporating SHAP-based prior weights, comprising an LSTM encoder, a variable-attention module (using normalized SHAP values as priors), a temporal-attention module, and a linear output layer. The LSTM component has two layers with 128 hidden units per layer, uses the tanh activation function, and applies a dropout rate of 0.5. Training uses mean squared error (MSE) as the loss function and the Adam optimizer with an initial learning rate of 0.001, a batch size of 64, and a maximum of 500 epochs. Adam parameters are $\beta_1 = 0.9$ and $\beta_2 = 0.999$, with a weight-decay coefficient of 1×10^{-5}. Considering GPU memory constraints, the training procedure employs batch-grouped training and dynamic cache clearing, leveraging torch.cuda.empty_cache() to release memory and ensure stable training.

To assess the contribution of the SHAP-guided mechanism to interpretability and generalization, ATLSTM was constructed as a control. This model shares the same architecture as the primary model, retaining both variable-level and temporal attention, but the attention weights in the variable-attention module are learned end-to-end without any prior guidance. Training parameters are kept identical to those of the SALSTM to ensure a fair comparison.

To comprehensively evaluate the predictive performance of the model, two key metrics were employed: Root Mean Square Error (RMSE) and the Coefficient of Determination (R^2). RMSE measures the average magnitude of the errors between predicted and observed values, with lower values indicating better predictive accuracy and closer alignment with actual measurements. In contrast, R^2 quantifies the proportion of variance in the observed data that is explained by the model, with values closer to 1 indicating stronger explanatory power. Together, RMSE and R^2 provide a complementary assessment of model performance from both error-based and variance-explanation perspectives, enabling a more robust evaluation of the model's accuracy and its capability to capture spatial patterns in yield distribution.

For hyperparameter tuning, both SALSTM and ATLSTM adopt a manual grid-search strategy, using RMSE and R^2 on the validation set to explore optimal combinations of network depth, hidden dimensions (64, 128, 256), and dropout ratios (0.3, 0.4, 0.5, 0.6). Conventional machine-learning models are tuned via GridSearchCV: the optimal XGBoost configuration is max_depth = 6, n_estimators = 350, and learning_rate = 0.1; the Random Forest (RF) uses n_estimators = 200 and max_features = sqrt; the SVR employs a radial basis function (RBF) kernel with $(0.1, 1, 10)$ and γ in $(scale,\ auto)$. The ANN is a three-layer fully connected network with 64 units in the hidden layer, ReLU activation, and 300 training epochs. For all models, RMSE and R^2 are computed on the training, validation, and test sets to comprehensively assess performance in terms of both fitting accuracy and generalization.

To benchmark the effectiveness of ISBI, an ablation variant of the SALSTM model was constructed in which ISBI was replaced by the original Enhanced Bloom Index (EBI). All model settings, feature inputs, and training procedures were kept identical to ensure comparability.

4. Results

4.1. Spatio-Temporal Distribution of Camellia oleifera Yield Prediction

Based on the feature-importance–guided Attention–LSTM model, yield predictions for *Camellia oleifera* from 2019 to 2023 were generated for the Hengyang region. As illustrated in Figure 6, the leave-one-year-out (LOYO) validation results yielded an R^2 of 0.7786 and a root mean square error (RMSE) of 0.5912 t/ha. To facilitate visualization and comparison of

spatial patterns, both observed and predicted yields were classified into seven categories, allowing a direct assessment of the model's ability to represent yield gradients across different productivity levels. Overall, the model effectively captures the broad spatial variability of *C. oleifera* yield in Hengyang, particularly the pronounced contrast between the high-yield central–southern hilly regions and the low-yield mountainous areas in the west and north. These results indicate that the proposed SALSTM framework is capable of recovering the dominant spatial structure of *C. oleifera* productivity even when the target year is excluded from the training process.

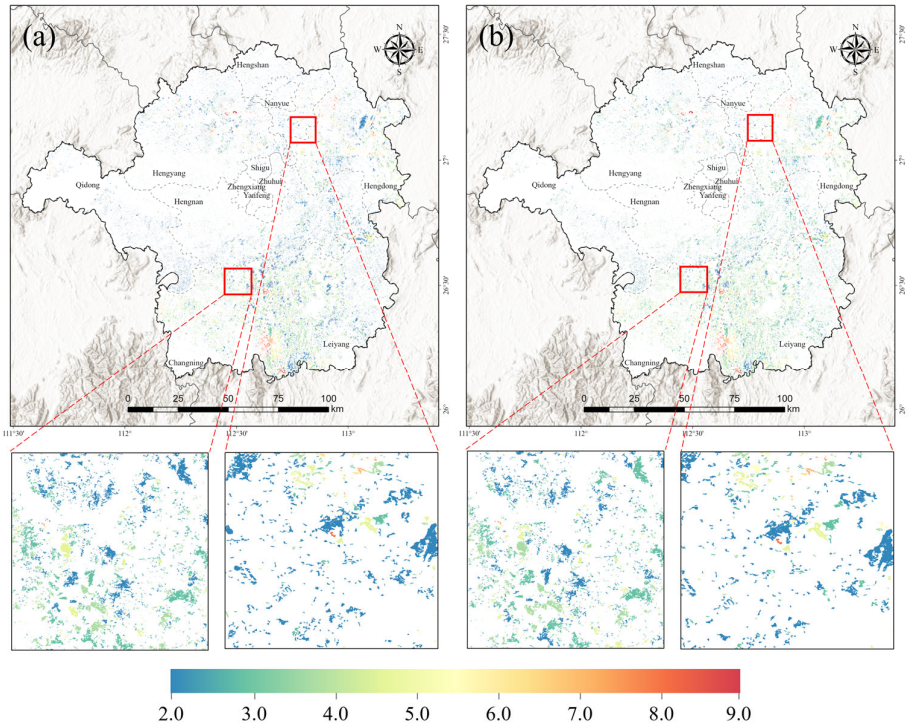


Figure 6. Cross-year generalization performance: observed yield (**a**) vs. SALSTM-predicted yield (**b**) distribution in 2022 under the LOYO setting: (**a**) refers to plot-level yields derived from the statistical downscaling framework, (**b**) presents the corresponding model predictions. Both maps were reclassified into seven yield classes (2.0–3.0, 3.0–4.0, 4.0–5.0, 5.0–6.0, 6.0–7.0, 7.0–8.0, and >8.0 t/ha) to ensure consistent visual comparison.

The LOYO experiment further demonstrates robust cross-year generalization performance, as major high-productivity belts are consistently identified, low-yield areas are correctly delineated, and the relative ranking of yield classes is largely preserved. The tendency to underestimate extreme high-yield parcels suggests that the model is more reliable in reproducing spatial yield patterns than in precisely capturing absolute yield magnitudes for years excluded from the training set.

From a spatial perspective, *Camellia oleifera* production exhibits pronounced variability across different topographic units. The hilly regions in the central and southern parts of the study area are characterized by moderate terrain undulations, with slopes predominantly ranging from 15° to 30°, conditions that are widely recognized as favorable for *C. oleifera* cultivation [3]. These areas consistently sustain high yield levels and constitute the core oil-producing belt of the region. The predicted yield distribution broadly corresponds to the observed spatial gradient, with high-yield parcels concentrated in the central and southern hilly zones, while comparatively lower yields occur in the mountainous areas of the north and west. Nevertheless, discrepancies remain in areas with complex terrain, where the model tends to underestimate yields in high-yield plots.

In contrast, the central–western region is characterized by gentler terrain but higher levels of urbanization. A large proportion of land in this area is allocated to construction and intensive agriculture, which constrains the extent of *Camellia oleifera* cultivation and results in comparatively lower yields. In the northern and western highland fringe areas, increased elevation and steeper slopes further reduce land suitability, leading to lower planting density and yield. In particular, localized prediction discrepancies in complex terrain zones may arise from fragmented topography, heterogeneous slope aspects, and mixed land-use patterns.

From a temporal perspective, Camellia oleifera production remained generally stable between 2019 and 2023, exhibiting minimal interannual variability, as illustrated in Figure 7. Major production areas consistently maintained high yield levels throughout the five-year period, demonstrating strong temporal stability in their productivity patterns. In contrast, certain peripheral regions, such as the eastern margin of Hengshan County and the southern margin of Leiyang City, experienced noticeable yield fluctuations in specific years. For example, southern Qidong County and southern Leiyang City showed pronounced yield declines in 2022, whereas in 2023, localized yield recovery patches appeared in northern Nanyue District and central Hengshan County.

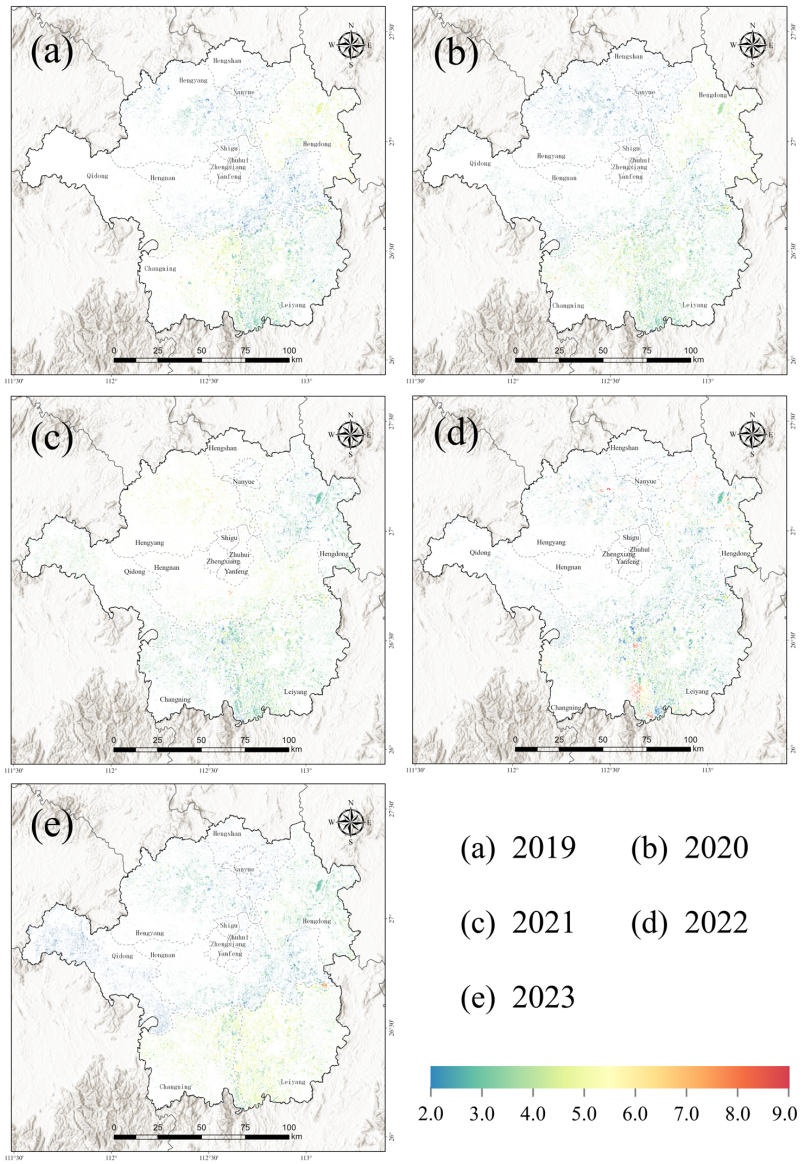


Figure 7. Multi-Year Forecast Results.

4.2. Feature Importance Interpretation

To investigate the contributions of different input variables to yield prediction within the proposed modeling framework, a feature attribution analysis was performed using the XGBoost model in conjunction with SHAP. SHAP values quantify the marginal contribution of each input feature to the model output under the learned data distribution, thereby providing a model-based assessment of feature relevance rather than a direct interpretation of underlying physiological processes.

Figure 8 presents the feature importance results derived using the SHAP method. The left panel illustrates the contribution distribution across different variable categories. Phenological variables represented by ISBI exhibit the highest overall contribution within the model, highlighting their dominant role in determining yield formation potential. Meteorological variables rank second in importance, underscoring their critical function in regulating yield dynamics from flowering to harvest. In contrast, SAVI and MXSPD show relatively low mean SHAP values, indicating a comparatively limited influence on model predictions within the current feature set. The right panel displays the SHAP summary plot, which depicts the distribution of SHAP values across all samples for the top 15 most influential features. ISBI during September–November occupies the highest positions in the ranking and exhibits a consistently right-skewed SHAP value distribution, suggesting that higher ISBI values are systematically associated with higher predicted yields. In comparison, several meteorological variables display dispersed, bidirectional SHAP distributions accompanied by complex color patterns, indicating that their effects on yield are phase-dependent and may either promote or constrain yield formation at different stages of the growth cycle.

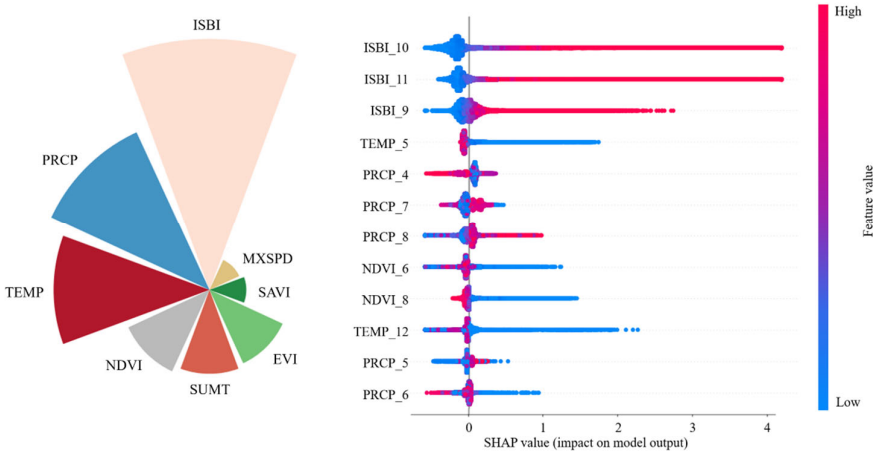


Figure 8. Feature importance results based on the SHAP method.

Figure 9 presents the correlation matrix of the top 10 key features selected based on SHAP importance, including the ISBI variables (September–November), representative meteorological variables, NDVI (July), and the original EBI (September–November) incorporated for comparison. Redundant variables with low importance were removed to enhance readability and interpretability.

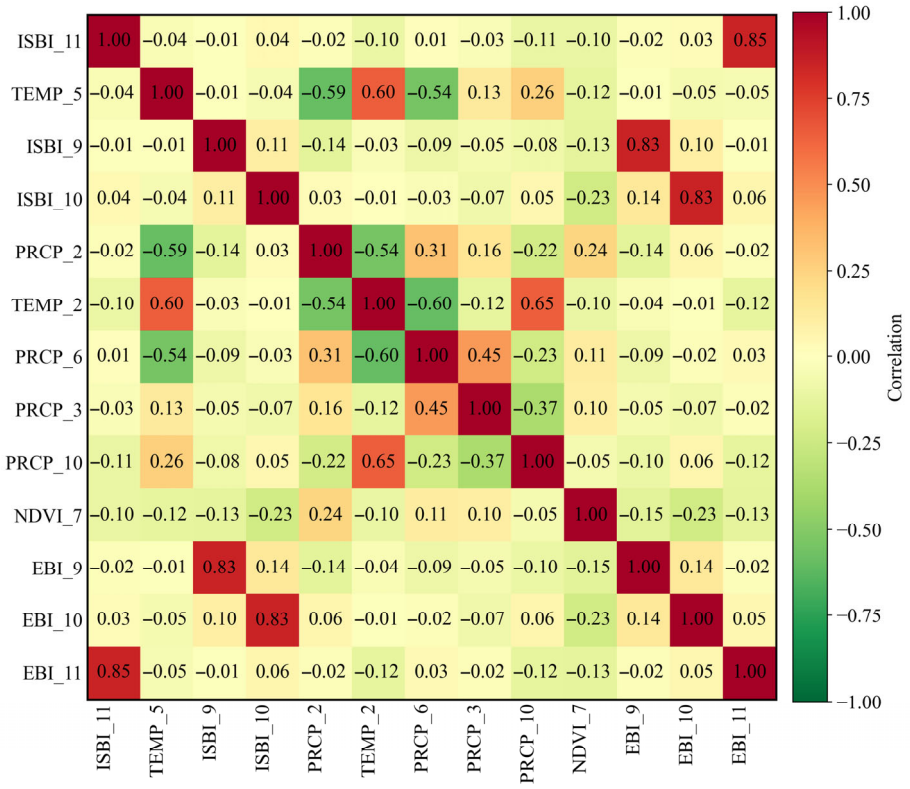


Figure 9. Top 10 most important features and their pairwise correlations, with both ISBI and original EBI included for comparison.

Overall, the correlation structure exhibits clear feature clusters rather than uniformly high correlations. ISBI variables show strong internal correlations, reflecting the temporal continuity of flowering intensity. Importantly, ISBI displays only weak correlations with NDVI, indicating that ISBI captures phenological signals that are distinct from conventional vegetation indices. In contrast, the original EBI variables exhibit notably lower correlations with meteorological variables and smaller covariance with ISBI, supporting the improvement achieved by the proposed ISBI.

For meteorological features, precipitation variables (PRCP) show moderate correlations among adjacent months, while exhibiting generally weak relationships with temperature (TEMP) or spectral variables. This suggests that precipitation contributes independent environmental information. TEMP variables also display moderate cross-temporal correlation, consistent with seasonal climate patterns.

NDVI_7 remains only weakly correlated with all other variables, confirming its limited sensitivity to flowering-related variability.

Overall, the refined correlation analysis shows that the ISBI contributes information that is largely independent of both conventional vegetation indices and environmental variables, indicating that it captures phenological signals not represented by traditional spectral features. Meteorological variables exhibit clear seasonal correlation structures, reflecting their intrinsic climatic continuity and aligning well with agronomic understanding of crop–environment interactions.

4.3. Temporal and Feature Attention Result

In the Attention–LSTM model, the attention mechanism dynamically assigns weights across both temporal steps and feature dimensions, thereby modulating how multi-source temporal inputs contribute to yield prediction. The distribution of attention weights shown in Figure 10 illustrates how the model internally allocates representational focus under the

learned data structure. This section examines the temporal and feature-wise patterns of attention weights and compares them with feature attribution results obtained from the XGBoost–SHAP analysis, with the aim of characterizing model behavior from a decision-making perspective.

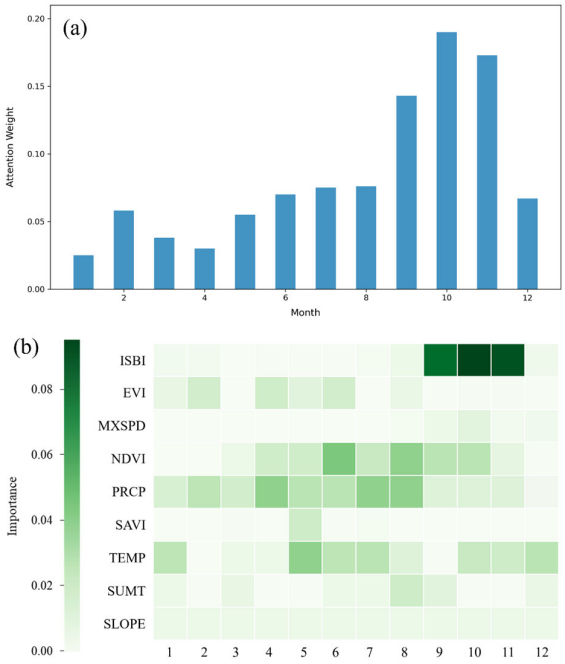


Figure 10. Average Time Attention Distribution Across Different Months. (**a**) Monthly attention weight distribution derived from the temporal attention module. (**b**) Attention weights assigned to different input features across the 12 monthly time steps, corresponding to ISBI, vegetation indices, meteorological variables, and topographic factors.

From a temporal perspective, attention weights exhibit clear phase-dependent variations across months. Overall, attention gradually increases over the annual cycle and peaks during September–November, with October receiving the highest average weight. This pattern is consistent with the phenological cycle of *Camellia oleifera*, as October–November corresponds to the key flowering period, during which ISBI effectively captures flowering density [67,68]. Importantly, elevated attention weights should be interpreted as reflecting the model's sensitivity to temporally informative inputs rather than as direct evidence of physiological dominance. In addition to the flowering period, moderate attention is also allocated to February and June–August, indicating that the model integrates information from multiple growth stages rather than relying on a single temporal window. This behavior suggests a cumulative decision-making process instead of a point-specific dependency, illustrating how the model distributes representational focus across the annual cycle during training.

At the feature dimension, Figure 10b illustrates the temporal variation in attention weights across different input variables. ISBI receives markedly higher attention during September–November, indicating that flowering-related spectral information is heavily emphasized by the model during this critical phenological period. Precipitation (PRCP) maintains relatively high attention throughout the year, particularly from May to August, reflecting its consistent utilization by the model under varying climatic conditions. Temperature (TEMP) exhibits elevated attention in January, May, and October, suggesting its relevance in specific seasonal contexts. As a static variable, SLOPE shows relatively uniform attention across months, indicating its role as a spatial contextual constraint rather than a temporally varying driver. MXSPD receives increased attention during October–November,

implying that wind-related information is more actively incorporated by the model during this stage; however, this pattern should be interpreted as a modeling preference rather than direct evidence of a causal effect.

A comparison between attention-based weighting and SHAP-derived feature attribution, as illustrated in Figure 11, reveals broad consistency in how the model prioritizes major variables such as ISBI, PRCP, and TEMP. This consistency reflects alignment between two complementary perspectives on model behavior rather than serving as independent validation. ISBI ranks highly in both attention and SHAP analyses, indicating that flowering-related inputs contribute substantially to model predictions, while PRCP and TEMP likewise exhibit stable importance across both approaches. However, discrepancies are observed for certain variables. NDVI receives relatively high attention weights but lower SHAP contributions, suggesting that although it influences intermediate representations within the network, its marginal contribution to the final predictions is limited. By contrast, EVI shows higher SHAP values but reduced attention weights, likely due to redundancy with other vegetation indices that leads to partial suppression during dynamic weighting. These differences highlight that attention weights characterize how the model allocates representational focus during information processing, whereas SHAP values quantify the contribution of features to output predictions. Taken together, these two perspectives provide complementary insights into model behavior without implying causal or mechanistic interpretations.

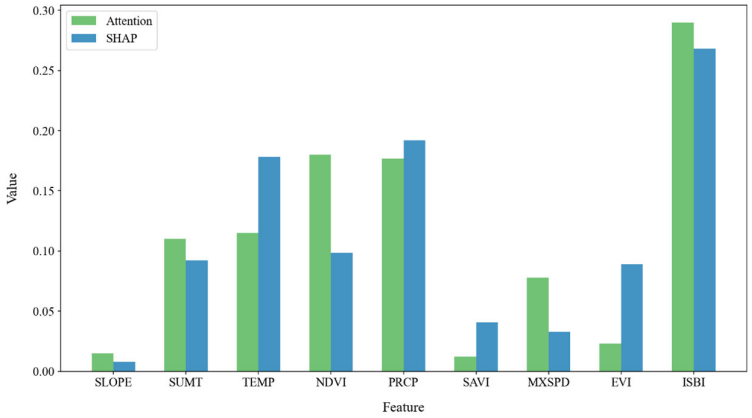


Figure 11. Comparison of Feature Importance Between Attention Mechanisms and SHAP.

4.4. Model Comparison

This study evaluated the performance of eight commonly used prediction models for remote sensing-based *Camellia oleifera* yield estimation. All models were trained and tested using identical input feature sets, with the available data split into training, validation, and test subsets at a ratio of 7:2:1. Table 2 provides a systematic comparison of model performance in terms of root mean square error (RMSE) and coefficient of determination (R^2) across the training, validation, and test datasets.

Table 2. Performance Comparison of LR, SVR, ANN, RF, XGBoost, LSTM, ATLSTM, and SALSTM Models.

Model	Training		Validation		Test	
	RMSE (t/ha)	**R^2**	**RMSE (t/ha)**	**R^2**	**RMSE (t/ha)**	**R^2**
LR	0.4681	0.8462	0.5910	0.7582	0.7642	0.6245
SVR	0.4963	0.8271	0.5807	0.7483	0.7872	0.6239
RF	0.3425	0.9251	0.3856	0.8221	0.6881	0.7298
ANN	0.3747	0.9104	0.4051	0.8042	0.6644	0.7342
XGBoost	0.3149	0.9678	0.3734	0.8724	0.5824	0.7645
LSTM	0.3658	0.9535	0.4258	0.8118	0.6858	0.7374
ATLSTM	0.3036	0.9690	0.3996	0.8639	0.5948	0.7694
SALSTM	0.3129	0.9639	0.3728	0.8769	**0.5738**	**0.7943**

Overall, the traditional linear models LR and SVR performed substantially worse than the other models across all evaluation stages. Their test-set RMSEs were 0.7642 t/ha and 0.7872 t/ha, respectively, with corresponding R^2 values of only 0.6245 and 0.6439, indicating limited capacity to capture nonlinear relationships inherent in the yield prediction task. In contrast, ensemble-based models such as RF and XGBoost achieved markedly improved prediction accuracy, with XGBoost exhibiting particularly strong performance. Its training-set R^2 reached 0.9678, and its test-set RMSE was 0.5824 t/ha, making it the best-performing non–deep learning model. The artificial neural network (ANN) also demonstrated robust and stable performance across all stages, with validation and test RMSEs consistently maintained at approximately 0.5 t/ha.

The LSTM model, which explicitly incorporates temporal sequence structures, exhibited improved predictive performance by reducing the validation-set RMSE to 0.4258 t/ha and increasing the test-set R^2 o 0.7373, thereby demonstrating its advantage in capturing the temporal dynamics of crop yields. Building on this foundation, the introduction of attention mechanisms further enhanced the model's ability to focus on critical time periods and influential variables. The Attention–LSTM (ATLSTM) model achieved a reduced validation-set RMSE of 0.3996 t/ha and a test-set RMSE of 0.5948 t/ha. Although its test performance was slightly inferior to that of XGBoost, ATLSTM offers improved interpretability through explicit temporal and feature weighting. Guided by SHAP-derived feature priors, the proposed SALSTM model demonstrated the best overall performance among all evaluated models. It achieved the lowest RMSE values across the training, validation, and test sets (0.3129, 0.3708, and 0.5738 t/ha, respectively), along with a test-set R^2 of 0.7943, which was the highest observed. These results indicate that SALSTM achieves an optimal balance between predictive accuracy, model stability, and generalization capability.

Figure 12 presents the 1:1 scatter plots for all models evaluated on the test dataset. The LR and SVR models exhibit substantial deviations from the 1:1 reference line, particularly in high-yield regions, where the point clouds display a pronounced fan-shaped dispersion and weak linear agreement, indicating systematic prediction bias (Figure 12a,b). In contrast, the RF and ANN models show comparatively narrower error bands, with point clouds more tightly clustered around the 1:1 line across several yield intervals, suggesting improved but still limited predictive stability (Figure 12c,d).

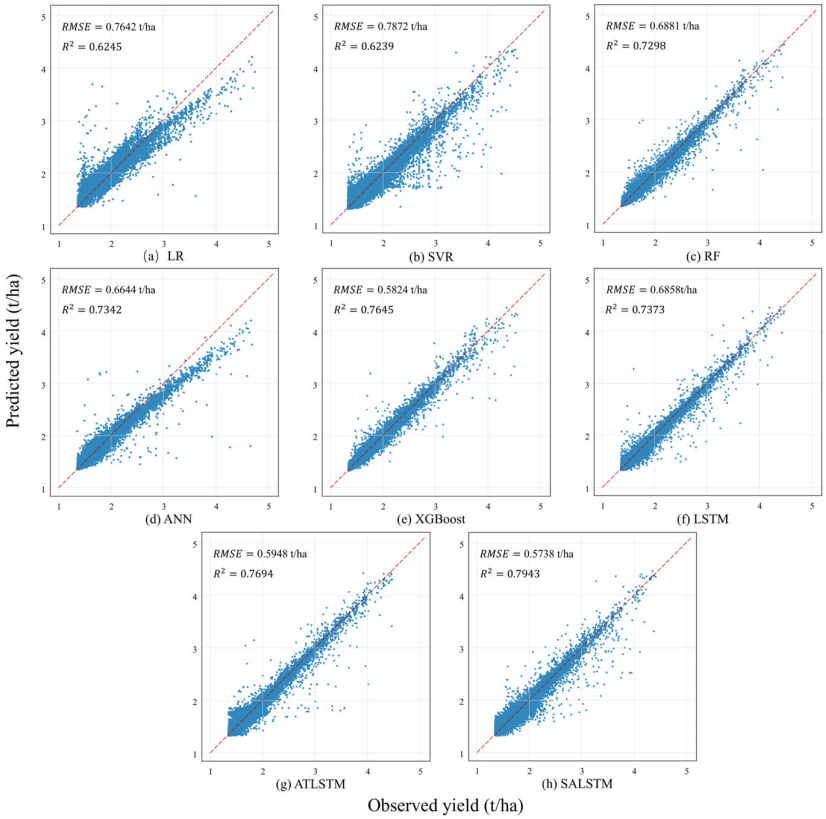


Figure 12. Scatter Plot of Predicted Yields from Different Models.

XGBoost further improves overall fitting performance relative to the preceding models, producing a visually tighter clustering of points in the medium-to-high yield range (Figure 12e). However, this apparent compactness is partly attributable to a regression-to-the-mean effect, whereby high yields tend to be underestimated and low yields overestimated. Although this effect reduces overall visual dispersion, it leads to increased prediction errors near the yield extremes. In comparison, the LSTM model better captures nonlinear relationships in the medium-to-low yield range and exhibits a clearer linear correspondence with observations; nevertheless, it still shows a tendency to overestimate extreme high-yield values (Figure 12f).

The ATLSTM model further reduces error dispersion by incorporating an attention mechanism, resulting in a more uniform distribution of predictions and a fitted slope that more closely aligns with the 1:1 reference line (Figure 12g). The SALSTM model achieves the highest quantitative accuracy among all evaluated models, particularly by mitigating systematic deviations at both low- and high-yield extremes. Although its point cloud is not as visually compact as that of XGBoost in the central yield range, SALSTM delivers more balanced performance across the full yield spectrum and yields the smallest overall prediction error (Figure 12h).

To further evaluate the contribution of the proposed ISBI, we conducted an ablation experiment in which ISBI was substituted with the original EBI while keeping all other modeling components unchanged. Table 3 summarizes the performance metrics of the two indices under the same SALSTM architecture.

Table 3. Performance comparison between SALSTM-ISBI and SALSTM-EBI under standard testing and leave-one-year-out (LOYO) evaluation.

Model	RMSE (t/ha)	R^2	RMSE (LOYO)	R^2 (LOYO)
SALSTM-ISBI	0.5738	0.7943	0.5912	0.7786
SALSTM-EBI	0.8245	0.6512	0.8450	0.6321
Improvement	−30.4%	+22.0%	−30.0%	+23.2%

Under standard testing, SALSTM-ISBI reduced RMSE from 0.8245 to 0.5738 t/ha (a 30.4% improvement) and increased R^2 from 0.6512 to 0.7943 (a 22.0% improvement). Similar benefits were observed in the LOYO evaluation, in which RMSE decreased from 0.8450 to 0.5912 t/ha (a 30.0% improvement) and R^2 increased from 0.6321 to 0.7786 (a 23.2% improvement). These results demonstrate that ISBI provides a more discriminative and robust flowering signal than EBI, particularly under interannual variability. ISBI enables more accurate representation of phenology-driven yield potential, resulting in meaningful gains in both predictive accuracy and temporal generalization.

5. Discussion

This study proposes a "potential–stress" yield estimation framework in which the Improved Spectral Bloom Index (ISBI) is employed as a key phenological indicator linked to yield potential and is integrated with multiple environmental variables representing climatic regulation. Based on the implementation of the SALSTM model, this framework does not merely learn a single empirical mapping between inputs and yield. Instead, it explicitly encourages the model to distinguish yield formation potential determined by phenological stages from subsequent environmental regulation, thereby aligning the modeling logic more closely with the underlying biological processes of *Camellia oleifera* growth. The core of the framework lies in the enhanced Spectral Bloom Index (ISBI), which strengthens the extraction of blooming signals and provides a phenological foundation for yield formation. Compared with the conventional Enhanced Bloom Index (EBI), ISBI more effectively suppresses the influence of the green canopy background, improves spectral sensitivity to pale and sparsely distributed camellia flowers, and offers a more reliable characterization of yield potential. The proposed SALSTM model demonstrates robust predictive performance for *C. oleifera* yield under the complex mountainous terrain of Hengyang City. By integrating SHAP-based feature attribution with temporal attention mechanisms, the model reveals complementary weighting patterns across variables and growth stages during prediction, thereby facilitating sensitivity analysis of phenological and environmental drivers without implying direct causal interpretation.

Systematic differences are evident between traditional machine learning models and deep learning approaches. Conventional machine learning methods tend to perform well within moderate yield ranges but often exhibit regression-to-the-mean behavior at yield extremes, resulting in systematic bias. In contrast, deep learning models are more effective at capturing temporal dependencies among flowering, fruit development, and environmental regulation. By integrating temporal attention mechanisms with SHAP-guided prior knowledge, the proposed SALSTM model achieves more balanced predictive performance across the full yield spectrum.

Environmental factors exert stage-specific regulatory effects on yield formation. Precipitation plays a critical role during bud break, flowering, and fruit enlargement stages [69]. Temperature influences multiple developmental phases, including floral differentiation, fruit growth, and pollination [70,71]. Strong wind events may reduce pollination efficiency or induce the abscission of flowers and young fruits, thereby affecting yield in the current season and potentially imposing delayed stress that increases production risks in

subsequent years [72]. Together, these factors act across multiple developmental stages, forming a characteristic cross-seasonal environmental regulation pathway. Final yield formation thus represents a dynamic response process, determined by flowering potential and subsequently modulated by prevailing environmental conditions.

From a temporal perspective, in addition to the pronounced weighting assigned to the September–November period, relatively elevated attention is also allocated to June–August. This pattern indicates that the model captures a multi-stage cumulative process consistent with established growth sequences, including flower bud differentiation, flowering, fruit development, and ripening. By emphasizing stage-specific contributions, this strategy avoids the tendency of conventional LSTM models to distribute attention uniformly across all time steps. At the spatial scale, although the SALSTM model effectively reproduces the spatial distribution and magnitude of yield variability, its ability to represent extreme high-productivity conditions remains limited. Nevertheless, the model maintains stable predictive performance across the primary production areas of Hengyang City, even under the drought conditions experienced in 2022 and 2023.

Nevertheless, uncertainties remain in the proposed framework. Except for 2022, yield labels were generated through statistical downscaling, which inevitably introduces uncertainty into the training data. Although the use of consistent processing procedures across years helps to mitigate systematic temporal biases, the limited availability of multi-year field observations constrains more rigorous uncertainty quantification. Future incorporation of longer-term field measurement datasets, together with more accurate and detailed camellia distribution maps, would enable improved error assessment and provide stronger validation of the proposed framework.

Several limitations of this study should be acknowledged. The current modeling framework does not explicitly account for cultivar-level heterogeneity, which may introduce regional biases in yield estimation. In addition, the exclusion of soil physicochemical properties and field management practices constrains the model's ability to explain fine-scale yield variability. Future studies that integrate richer agroecological information and improve the representativeness of training samples would strengthen the physical grounding and explanatory power of the proposed framework.

The multi-temporal predictors employed in this study exhibit varying degrees of correlation between consecutive months, stemming from the inherent seasonal continuity of meteorological and vegetation conditions. This inevitably introduces uncertainty into interpretability analyses. Under such correlated inputs, SHAP attribution does not yield a mathematically unique solution, as multiple features share overlapping information, potentially redistributing importance among correlated variables. Consequently, the SHAP results presented herein should be interpreted as reflecting the model's sensitivity to information from different features, rather than as estimates of the independent contribution of individual variables. Whilst correlations do affect the precision of attribution, they do not undermine the core conclusion of this study: phenological potential derived from flowering remains the dominant factor in yield formation, followed by the environmental regulation of key developmental stages. Moreover, the interpretability analysis in this study aims to reveal stable sensitivity patterns and stage-dependent regulatory signals, rather than ascribe unique and separable causal effects to any correlated predictors.

6. Conclusions

This study developed an interpretable deep learning framework for large-scale yield estimation of *Camellia oleifera* by integrating phenological and environmental driving factors within a "potential–stress" modeling concept. Multi-source datasets were used to construct monthly time-series inputs, and the proposed SALSTM model incorporated the Improved

Spectral Bloom Index (ISBI) as a phenology-driven indicator of yield potential, together with environmental variables acting as stress regulators. This design enabled simultaneous improvements in predictive accuracy and model interpretability. Feature importance analysis revealed that ISBI contributed most substantially to yield prediction, highlighting flowering intensity as the dominant determinant of yield potential. Average temperature and precipitation during the flowering-to-fruiting period ranked next in importance, underscoring the critical regulatory roles of thermal and moisture conditions in yield realization. Attention-weight analysis further showed that the September–November period received the highest temporal attention, corresponding to key flowering and pollination stages, while moderate attention during April and June–August reflected the influence of early bud break and fruit expansion on yield accumulation.

In comparative model evaluation, the proposed SALSTM achieved superior predictive performance (RMSE = 0.5738 t/ha, R^2 = 0.7943) relative to all baseline models. These results demonstrate that embedding SHAP-derived prior information into the attention mechanism effectively enhances model stability, generalization capability, and interpretability. Spatially, high-yield areas were primarily concentrated in the hilly terrain of central and southern Hengyang, characterized by moderate slopes, favorable thermohygric conditions, and relatively standardized management practices. In contrast, the northern mountainous regions and western plains exhibited comparatively lower yields due to topographic constraints and land-use limitations.

Overall, the proposed phenology-driven yield estimation framework provides a transparent and biologically grounded paradigm for remote sensing-based yield modeling of perennial oilseed crops. It offers robust methodological support for digital yield monitoring and precision management of *Camellia oleifera* plantations and has strong potential for extension to other perennial crops with similar phenological characteristics.

Author Contributions: Conceptualization, T.S. and S.C.; methodology, T.S. and X.L. (Xiangnan Liu); software, X.L. (Xia Lu); validation, L.P., T.S. and X.F.; formal analysis, L.P.; investigation, T.S.; resources, X.F.; data curation, X.L. (Xiangnan Liu); writing—original draft preparation, T.S.; writing—review and editing, M.L. and S.C.; visualization, L.P. and X.L. (Xia Lu); supervision, X.L. (Xiangnan Liu); project administration, S.C.; funding acquisition, M.L. All authors have read and agreed to the published version of the manuscript.

Funding: This research was supported by Hunan Provincial Department of Finance, 2025 Procurement Plan (No. 000346).

Data Availability Statement: Due to institutional restrictions and agreements with the data providers, the datasets used in this study are not publicly available. However, the data can be obtained from the corresponding author upon reasonable request.

Acknowledgments: During the preparation of this work, the authors used ChatGPT 5.1 solely for language polishing to improve readability. After using this tool, the authors carefully reviewed and edited the text as needed and take full responsibility for the content of this publication.

Conflicts of Interest: The authors declare that they have no known competing financial interests or personal relationships that could have appeared to influence the work reported in this paper.

References

1. Yang, L.; Gao, C.; Xie, J.; Qiu, J.; Deng, Q.; Zhou, Y.; Liao, D.; Deng, C. Fruit economic characteristics and yields of 40 superior *Camellia oleifera* Abel plants in the low-hot valley area of Guizhou Province, China. *Sci. Sci. Rep.* **2022**, *12*, 7068. [CrossRef] [PubMed]
2. Zhang, F.; Zhu, F.; Chen, B.; Su, E.; Chen, Y.; Cao, F. Composition, bioactive substances, extraction technologies and the influences on characteristics of Camellia oleifera oil: A review. *Food Res. Int.* **2022**, *156*, 111159. [CrossRef] [PubMed]

3. Li, Y.; Yan, E.; Jiang, J.; Cao, D.; Mo, D. Investigating the identification and spatial distribution characteristics of camellia oleifera plantations using high-resolution imagery. *Remote Sens.* **2023**, *15*, 5218. [CrossRef]
4. Wang, R. Production, marketing, import and export of grain and oil in China in 2022. *China Oils Fats* **2023**, *48*, 1–7.
5. Joshi, A.; Pradhan, B.; Gite, S.; Chakraborty, S. Remote-sensing data and deep-learning techniques in crop mapping and yield prediction: A systematic review. *Remote Sens.* **2023**, *15*, 2014. [CrossRef]
6. He, J.; He, F.; Kang, W.; Wu, X.; Wang, J.; Liao, Q.; Yan, W. Implications for yield enhancement of Camellia oleifera plantation in Hunan Province: Based on distribution and yield influencing factors. *Ind. Crops Prod.* **2025**, *234*, 121486. [CrossRef]
7. Chen, Y.; Zheng, J.; Yang, Z.; Xu, C.; Liao, P.; Pu, S.; El-Kassaby, Y.A.; Feng, J. Role of soil nutrient elements transport on *Camellia oleifera* yield under different soil types. *BMC Plant Biol.* **2023**, *23*, 378. [CrossRef]
8. Liu, J.; Wu, L.; Chen, D.; Yu, Z.; Wei, C. Development of a soil quality index for *Camellia oleifera* forestland yield under three different parent materials in Southern China. *Soil Tillage Res.* **2018**, *176*, 45–50. [CrossRef]
9. Kamir, E.; Waldner, F.; Hochman, Z. Estimating wheat yields in Australia using climate records, satellite image time series and machine learning methods. *ISPRS J. Photogramm. Remote Sens.* **2020**, *160*, 124–135. [CrossRef]
10. Lobell, D.B.; Thau, D.; Seifert, C.; Engle, E.; Little, B. A scalable satellite-based crop yield mapper. *Remote Sens. Environ.* **2015**, *164*, 324–333. [CrossRef]
11. Atzberger, C. Advances in remote sensing of agriculture: Context description, existing operational monitoring systems and major information needs. *Remote Sens.* **2013**, *5*, 949–981. [CrossRef]
12. You, J.; Li, X.; Low, M.; Lobell, D.; Ermon, S. Deep gaussian process for crop yield prediction based on remote sensing data. In Proceedings of the AAAI Conference on Artificial Intelligence, San Francisco, CA, USA, 4–9 February 2017.
13. Kang, Y.; Özdoğan, M. Field-level crop yield mapping with Landsat using a hierarchical data assimilation approach. *Remote Sens. Environ.* **2019**, *228*, 144–163. [CrossRef]
14. Doraiswamy, P.C.; Hatfield, J.L.; Jackson, T.J.; Akhmedov, B.; Prueger, J.; Stern, A. Crop condition and yield simulations using Landsat and MODIS. *Remote Sens. Environ.* **2004**, *92*, 548–559. [CrossRef]
15. Sakamoto, T. Incorporating environmental variables into a MODIS-based crop yield estimation method for United States corn and soybeans through the use of a random forest regression algorithm. *ISPRS J. Photogramm. Remote Sens.* **2020**, *160*, 208–228. [CrossRef]
16. Li, Y.; Zeng, H.; Zhang, M.; Wu, B.; Zhao, Y.; Yao, X.; Cheng, T.; Qin, X.; Wu, F. A county-level soybean yield prediction framework coupled with XGBoost and multidimensional feature engineering. *Int. J. Appl. Earth Obs. Geoinf.* **2023**, *118*, 103269. [CrossRef]
17. Duan, K.; Vrieling, A.; Schlund, M.; Nidumolu, U.B.; Ratcliff, C.; Collings, S.; Nelson, A. Detection and attribution of cereal yield losses using Sentinel-2 and weather data: A case study in South Australia. *ISPRS J. Photogramm. Remote Sens.* **2024**, *213*, 33–52. [CrossRef]
18. Chen, L.; Letu, H.; Fan, M.; Shang, H.; Tao, J.; Wu, L.; Zhang, Y.; Yu, C.; Gu, J.; Zhang, N. An introduction to the Chinese high-resolution Earth observation system: Gaofen-1 ~ 7 civilian satellites. *J. Remote Sens.* **2022**, *2022*, 9769536. [CrossRef]
19. Huang, J.; Gómez-Dans, J.L.; Huang, H.; Ma, H.; Wu, Q.; Lewis, P.E.; Liang, S.; Chen, Z.; Xue, J.-H.; Wu, Y. Assimilation of remote sensing into crop growth models: Current status and perspectives. *Agric. For. Meteorol.* **2019**, *276*, 107609. [CrossRef]
20. Van Klompenburg, T.; Kassahun, A.; Catal, C. Crop yield prediction using machine learning: A systematic literature review. *Comput. Electron. Agric.* **2020**, *177*, 105709. [CrossRef]
21. Darwin, B.; Dharmaraj, P.; Prince, S.; Popescu, D.E.; Hemanth, D.J. Recognition of bloom/yield in crop images using deep learning models for smart agriculture: A review. *Agronomy* **2021**, *11*, 646. [CrossRef]
22. Jones, J.W.; Hoogenboom, G.; Porter, C.H.; Boote, K.J.; Batchelor, W.D.; Hunt, L.A.; Wilkens, P.W.; Singh, U.; Gijsman, A.J.; Ritchie, J.T. The DSSAT cropping system model. *Eur. J. Agron.* **2003**, *18*, 235–265. [CrossRef]
23. Heinen, M.; Mulder, M.; van Dam, J.; Bartholomeus, R.; van Lier, Q.d.J.; de Wit, J.; de Wit, A.; Hack-ten Broeke, M. SWAP 50 years: Advances in modelling soil-water-atmosphere-plant interactions. *Agric. Water Manag.* **2024**, *298*, 108883. [CrossRef]
24. Holzworth, D.P.; Huth, N.I.; deVoil, P.G.; Zurcher, E.J.; Herrmann, N.I.; McLean, G.; Chenu, K.; van Oosterom, E.J.; Snow, V.; Murphy, C. APSIM–evolution towards a new generation of agricultural systems simulation. *Environ. Model. Softw.* **2014**, *62*, 327–350. [CrossRef]
25. De Wit, A.; Boogaard, H.; Fumagalli, D.; Janssen, S.; Knapen, R.; van Kraalingen, D.; Supit, I.; van der Wijngaart, R.; van Diepen, K. 25 years of the WOFOST cropping systems model. *Agric. Syst.* **2019**, *168*, 154–167. [CrossRef]
26. Huang, J.; Song, J.; Huang, H.; Zhuo, W.; Niu, Q.; Wu, S.; Ma, H.; Liang, S. Progress and perspectives in data assimilation algorithms for remote sensing and crop growth model. *Sci. Remote Sens.* **2024**, *10*, 100146. [CrossRef]
27. Pan, H.; Chen, Z.; de Wit, A.; Ren, J. Joint assimilation of leaf area index and soil moisture from sentinel-1 and sentinel-2 data into the WOFOST model for winter wheat yield estimation. *Sensors* **2019**, *19*, 3161. [CrossRef]
28. Brandt, P.; Beyer, F.; Borrmann, P.; Möller, M.; Gerighausen, H. Ensemble learning-based crop yield estimation: A scalable approach for supporting agricultural statistics. *GISci. Remote Sens.* **2024**, *61*, 2367808. [CrossRef]

29. Prasad, A.K.; Chai, L.; Singh, R.P.; Kafatos, M. Crop yield estimation model for Iowa using remote sensing and surface parameters. *Int. J. Appl. Earth Obs. Geoinf.* **2006**, *8*, 26–33. [CrossRef]
30. Balaghi, R.; Tychon, B.; Eerens, H.; Jlibene, M. Empirical regression models using NDVI, rainfall and temperature data for the early prediction of wheat grain yields in Morocco. *Int. J. Appl. Earth Obs. Geoinf.* **2008**, *10*, 438–452. [CrossRef]
31. Jaafar, H.H.; Ahmad, F.A. Crop yield prediction from remotely sensed vegetation indices and primary productivity in arid and semi-arid lands. *Int. J. Remote Sens.* **2015**, *36*, 4570–4589. [CrossRef]
32. Rivera-Caicedo, J.P.; Verrelst, J.; Muñoz-Marí, J.; Camps-Valls, G.; Moreno, J. Hyperspectral dimensionality reduction for biophysical variable statistical retrieval. *ISPRS J. Photogramm. Remote Sens.* **2017**, *132*, 88–101. [CrossRef]
33. Carbajal, M.; Jones, D.; Williams, C.; Nelson, N.G. In-season yield forecasting using multitemporal remote sensing environmental observations and machine learning: Applications for sweetpotato in North Carolina, USA. *Eur. J. Agron.* **2026**, *172*, 127818. [CrossRef]
34. Cheng, E.; Zhang, B.; Peng, D.; Zhong, L.; Yu, L.; Liu, Y.; Xiao, C.; Li, C.; Li, X.; Chen, Y. Wheat yield estimation using remote sensing data based on machine learning approaches. *Front. Plant Sci.* **2022**, *13*, 1090970. [CrossRef] [PubMed]
35. Zhang, L.; Li, C.; Wu, X.; Xiang, H.; Jiao, Y.; Chai, H. BO-CNN-BiLSTM deep learning model integrating multisource remote sensing data for improving winter wheat yield estimation. *Front. Plant Sci.* **2024**, *15*, 1500499. [CrossRef] [PubMed]
36. Zhou, W.; Liu, Y.; Ata-Ul-Karim, S.T.; Ge, Q.; Li, X.; Xiao, J. Integrating climate and satellite remote sensing data for predicting county-level wheat yield in China using machine learning methods. *Int. J. Appl. Earth Obs. Geoinf.* **2022**, *111*, 102861. [CrossRef]
37. Lyu, Y.; Wang, P.; Bai, X.; Li, X.; Ye, X.; Hu, Y.; Zhang, J. Machine learning techniques and interpretability for maize yield estimation using Time-Series images of MODIS and Multi-Source data. *Comput. Electron. Agric.* **2024**, *222*, 109063. [CrossRef]
38. Mateo-Sanchis, A.; Adsuara, J.E.; Piles, M.; Munoz-Marí, J.; Perez-Suay, A.; Camps-Valls, G. Interpretable long short-term memory networks for crop yield estimation. *IEEE Geosci. Remote Sens. Lett.* **2023**, *20*, 2501105. [CrossRef]
39. Paudel, D.; De Wit, A.; Boogaard, H.; Marcos, D.; Osinga, S.; Athanasiadis, I.N. Interpretability of deep learning models for crop yield forecasting. *Comput. Electron. Agric.* **2023**, *206*, 107663. [CrossRef]
40. Yang, B.; Zhu, W.; Rezaei, E.E.; Li, J.; Sun, Z.; Zhang, J. The optimal phenological phase of maize for yield prediction with high-frequency UAV remote sensing. *Remote Sens.* **2022**, *14*, 1559. [CrossRef]
41. Wang, F.; Yao, X.; Xie, L.; Zheng, J.; Xu, T. Rice yield estimation based on vegetation index and florescence spectral information from UAV hyperspectral remote sensing. *Remote Sens.* **2021**, *13*, 3390. [CrossRef]
42. Tombesi, S.; Lampinen, B.D.; Metcalf, S.; DeJong, T.M. Yield in almond is related more to the abundance of flowers than the relative number of flowers that set fruit. *Calif. Agric.* **2017**, *71*, 2. [CrossRef]
43. Gong, Z.; Ge, W.; Guo, J.; Liu, J. Satellite remote sensing of vegetation phenology: Progress, challenges, and opportunities. *ISPRS J. Photogramm. Remote Sens.* **2024**, *217*, 149–164. [CrossRef]
44. Landmann, T.; Piiroinen, R.; Makori, D.M.; Abdel-Rahman, E.M.; Makau, S.; Pellikka, P.; Raina, S.K. Application of hyperspectral remote sensing for flower mapping in African savannas. *Remote Sens. Environ.* **2015**, *166*, 50–60. [CrossRef]
45. Gonzales, D.; Hempel de Ibarra, N.; Anderson, K. Remote sensing of floral resources for pollinators—New horizons from satellites to drones. *Front. Ecol. Evol.* **2022**, *10*, 869751. [CrossRef]
46. Yuan, W.; Hua, W.; Heinemann, P.H.; He, L. UAV photogrammetry-based apple orchard blossom density estimation and mapping. *Horticulturae* **2023**, *9*, 266. [CrossRef]
47. Chen, B.; Jin, Y.; Brown, P. An enhanced bloom index for quantifying floral phenology using multi-scale remote sensing observations. *ISPRS J. Photogramm. Remote Sens.* **2019**, *156*, 108–120. [CrossRef]
48. Chakraborty, M.; Pourreza, A.; Zhang, X.; Jafarbiglu, H.; Shackel, K.A.; DeJong, T. Early almond yield forecasting by bloom mapping using aerial imagery and deep learning. *Comput. Electron. Agric.* **2023**, *212*, 108063. [CrossRef]
49. Dixon, D.J.; Callow, J.N.; Duncan, J.M.; Setterfield, S.A.; Pauli, N. Satellite prediction of forest flowering phenology. *Remote Sens. Environ.* **2021**, *255*, 112197. [CrossRef]
50. Zang, Y.; Chen, X.; Chen, J.; Tian, Y.; Shi, Y.; Cao, X.; Cui, X. Remote sensing index for mapping canola flowers using MODIS data. *Remote Sens.* **2020**, *12*, 3912. [CrossRef]
51. Fernando, H.; Ha, T.; Attanayake, A.; Benaragama, D.; Nketia, K.A.; Kanmi-Obembe, O.; Shirtliffe, S.J. High-resolution flowering index for canola yield modelling. *Remote Sens.* **2022**, *14*, 4464. [CrossRef]
52. Shirsath, P.B.; Sehgal, V.K.; Aggarwal, P.K. Downscaling regional crop yields to local scale using remote sensing. *Agriculture* **2020**, *10*, 58. [CrossRef]
53. Huete, A.R. A soil-adjusted vegetation index (SAVI). *Remote Sens. Environ.* **1988**, *25*, 295–309. [CrossRef]
54. Van Ittersum, M.K.; Cassman, K.G.; Grassini, P.; Wolf, J.; Tittonell, P.; Hochman, Z. Yield gap analysis with local to global relevance—A review. *Field Crops Res.* **2013**, *143*, 4–17. [CrossRef]
55. Yaoming, L.; Jiangping, P.; Yuan, L. Climatic Suitability for *Camellia oleifera* Production in Shaoyang, Hunan. *J. Agric.* **2020**, *10*, 62.
56. Van Wart, J.; Grassini, P.; Cassman, K.G. Impact of derived global weather data on simulated crop yields. *Glob. Change Biol.* **2013**, *19*, 3822–3834. [CrossRef]

57. Lundberg, S.M.; Lee, S.-I. A unified approach to interpreting model predictions. *Adv. Neural Inf. Process. Syst.* **2017**, *30*.
58. Graham, J.; Sheng, V.S. SHAP Informed Neural Network. *Mathematics* **2025**, *13*, 849. [CrossRef]
59. Karpatne, A.; Atluri, G.; Faghmous, J.H.; Steinbach, M.; Banerjee, A.; Ganguly, A.; Shekhar, S.; Samatova, N.; Kumar, V. Theory-guided data science: A new paradigm for scientific discovery from data. *IEEE Trans. Knowl. Data Eng.* **2017**, *29*, 2318–2331. [CrossRef]
60. Qin, Y.; Song, D.; Chen, H.; Cheng, W.; Jiang, G.; Cottrell, G. A dual-stage attention-based recurrent neural network for time series prediction. *arXiv* **2017**, arXiv:1704.02971.
61. Chen, T.; Guestrin, C. Xgboost: A scalable tree boosting system. In Proceedings of the 22nd ACM SIGKDD International Conference on Knowledge Discovery and Data Mining, San Francisco, CA, USA, 13–17 August 2016; pp. 785–794.
62. Hochreiter, S.; Schmidhuber, J. Long short-term memory. *Neural Comput.* **1997**, *9*, 1735–1780. [CrossRef]
63. Gers, F.A.; Schmidhuber, J.; Cummins, F. Learning to forget: Continual prediction with LSTM. *Neural Comput.* **2000**, *12*, 2451–2471. [CrossRef] [PubMed]
64. Smola, A.J.; Schölkopf, B. A tutorial on support vector regression. *Stat. Comput.* **2004**, *14*, 199–222. [CrossRef]
65. Goodfellow, I.; Bengio, Y.; Courville, A.; Bengio, Y. *Deep Learning*; MIT Press: Cambridge, MA, USA, 2016; Volume 1.
66. Breiman, L. Random forests. *Mach. Learn.* **2001**, *45*, 5–32. [CrossRef]
67. Lu, Y.; Si, Y.; Zhang, L.; Sun, Y.; Su, S. Effects of canopy position and microclimate on fruit development and quality of *Camellia oleifera*. *Agronomy* **2022**, *12*, 2158. [CrossRef]
68. Deng, Q.; Li, J.; Gao, C.; Cheng, J.; Deng, X.; Jiang, D.; Li, L.; Yan, P. New perspective for evaluating the main *Camellia oleifera* cultivars in China. *Sci. Rep.* **2020**, *10*, 20676. [CrossRef]
69. Kozlowski, T. Reduction in yield of forest and fruit trees by water and temperature stress. In *Crop Reactions to Water and Temperature Stresses in Humid, Temperate Climates*; CRC Press: Boca Raton, FL, USA, 2019; pp. 67–88.
70. Yadav, S.; Korat, J.; Yadav, S.; Mondal, K.; Kumar, A.; Kumar, S.; Kumar, S. Impacts of climate change on fruit crops: A comprehensive review of physiological, phenological, and pest-related responses. *Int. J. Environ. Clim. Change* **2023**, *13*, 363–371. [CrossRef]
71. Medda, S.; Fadda, A.; Mulas, M. Influence of climate change on metabolism and biological characteristics in perennial woody fruit crops in the Mediterranean environment. *Horticulturae* **2022**, *8*, 273. [CrossRef]
72. Maeda, T.; Hiraiwa, M.K.; Shimomura, Y.; Oe, T. Weather conditions affect pollinator activity, fruit set rate, and yield in Japanese apricot. *Sci. Hortic.* **2023**, *307*, 111522. [CrossRef]

Disclaimer/Publisher's Note: The statements, opinions and data contained in all publications are solely those of the individual author(s) and contributor(s) and not of MDPI and/or the editor(s). MDPI and/or the editor(s) disclaim responsibility for any injury to people or property resulting from any ideas, methods, instructions or products referred to in the content.